



HAL
open science

Strong coupling to magnetic fluctuations in the charge dynamics of iron-based superconductors

Jason Hancock, S. I. Mirzaei, J. Gillett, S. E. Sebastian, Jérémie Teyssier, Romain Viennois, Enrico Giannini, Dirk van Der Marel

► **To cite this version:**

Jason Hancock, S. I. Mirzaei, J. Gillett, S. E. Sebastian, Jérémie Teyssier, et al.. Strong coupling to magnetic fluctuations in the charge dynamics of iron-based superconductors. *Physical Review B: Condensed Matter and Materials Physics (1998-2015)*, 2010, 82, pp.014523. 10.1103/PhysRevB.82.014523 . hal-00528175

HAL Id: hal-00528175

<https://hal.science/hal-00528175>

Submitted on 7 Jun 2021

HAL is a multi-disciplinary open access archive for the deposit and dissemination of scientific research documents, whether they are published or not. The documents may come from teaching and research institutions in France or abroad, or from public or private research centers.

L'archive ouverte pluridisciplinaire **HAL**, est destinée au dépôt et à la diffusion de documents scientifiques de niveau recherche, publiés ou non, émanant des établissements d'enseignement et de recherche français ou étrangers, des laboratoires publics ou privés.

Strong coupling to magnetic fluctuations in the charge dynamics of iron-based superconductors

J. N. Hancock,¹ S. I. Mirzaei,¹ J. Gillett,² S. E. Sebastian,² J. Teyssier,¹ R. Viennois,¹ E. Giannini,¹ and D. van der Marel¹

¹*Département de Physique de la Matière Condensée, Université de Genève, quai Ernest-Ansermet 24, CH 1211 Genève 4, Switzerland*

²*Cavendish Laboratory, Cambridge University, J. J. Thomson Avenue, Cambridge CB3 0HE, United Kingdom*

(Received 28 April 2010; revised manuscript received 30 June 2010; published 16 July 2010)

We present a comprehensive comparison of the infrared charge response of two systems, characteristic of classes of the 122 pnictide (SrFe_2As_2) and 11 chalcogenide ($\text{Fe}_{1.087}\text{Te}$) Fe compounds with magnetically ordered ground states. In the 122 system, the magnetic phase shows a decreased plasma frequency and scattering, and associated appearance of strong midinfrared features. The 11 system, with a different magnetic-ordering pattern, also shows decreased scattering, but an increase in the plasma frequency while no clear midinfrared features appear below the ordering temperature. We suggest how this marked contrast can be understood in terms of the diverse magnetic-ordering patterns of the ground state and conclude that while the high-temperature phases of these systems are similar, magnetic order strongly affects the charge dynamical response. In addition, we propose an optical-absorption mechanism which appears to be consistent with information gained from several different experiments.

DOI: [10.1103/PhysRevB.82.014523](https://doi.org/10.1103/PhysRevB.82.014523)

PACS number(s): 74.70.Xa, 74.25.Gz

I. INTRODUCTION

The iron pnictide or chalcogenide systems have often been compared to the cuprates based on proximity of magnetism to superconductivity. However, it is not clear whether these two classes of iron systems belong to the same universality class, given the notably different magnetic-ordering pattern of the parent compound ground states. Below $T_{ms} = 67$ K, the “11” chalcogenide $\text{Fe}_{1.087}\text{Te}$ undergoes a magnetostructural phase transition into a bidagonal magnetically ordered ground state [Fig. 1(a)] with a large moment of $\sim 2\mu_B$.¹⁻³ In contrast, the “122” pnictide SrFe_2As_2 ($T_{ms} = 190$ K) orders in a smaller moment, vertical-stripe pattern⁴ [Fig. 1(b)], common to the parent compounds of the type XFe_2As_2 and related compounds isostructural to LaFePO . Both systems can be driven superconducting by chemical substitution^{5,6} and pressure.^{7,8} Formal valence counting gives the same nominal Fe valence while electronic structure⁹⁻¹¹ and angle-resolved photoemission (ARPES) (Refs. 12 and 13) results suggest topological equivalence to the Fermi surfaces in the high-temperature, paramagnetic phase.

II. EXPERIMENTAL

Large samples of $\text{Fe}_{1.087}\text{Te}$ and SrFe_2As_2 were grown using the Bridgman¹⁴ and flux¹⁵ methods, respectively. Single-crystalline platelets were then characterized by magnetometry, x-ray diffraction, and resistivity measurements. Optical data were collected using a combination reflectivity and ellipsometry techniques. Figures 1(e) and 1(f) show the optical conductivity $\sigma_1(\omega) = \text{Re} \sigma(\omega)$ for $\text{Fe}_{1.087}\text{Te}$ and SrFe_2As_2 above and below their magnetostructural transition temperatures. Strong infrared changes accompany the transition in SrFe_2As_2 and at low temperature clear midinfrared features appear at 550 and 1300 cm^{-1} , qualitatively consistent with previous studies.¹⁶⁻¹⁸ Approaching T_{ms} from below, a marked weakening and softening of these features is apparent. In contrast, $\text{Fe}_{1.087}\text{Te}$ shows far weaker temperature de-

pendence, and only a broad, flat background free of sharp peaks, similar to the high-temperature phase of SrFe_2As_2 . Electronic-structure calculations performed within the local-density approximation¹⁹ predict more distinct features in

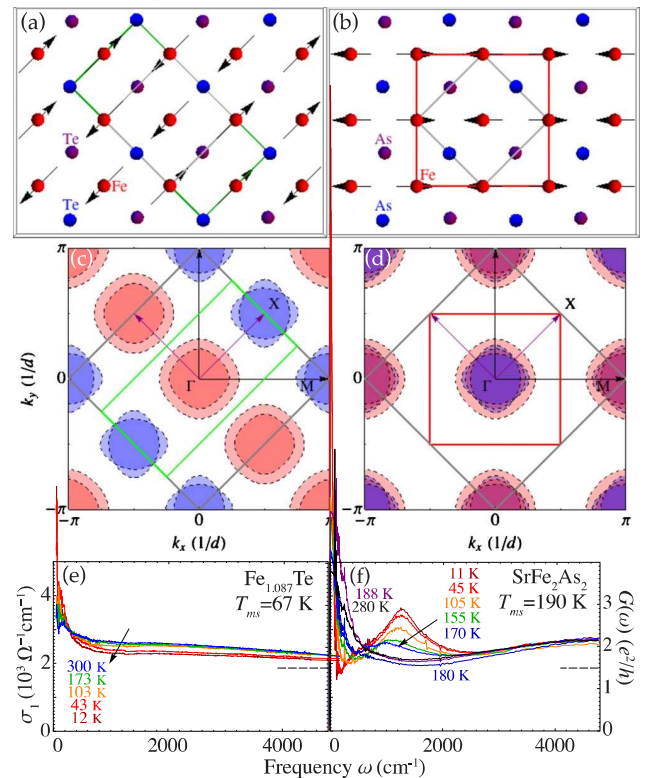


FIG. 1. (Color online) Low-temperature magnetic structure of (a) $\text{Fe}_{1.087}\text{Te}$ and (b) SrFe_2As_2 . [(c) and (d)] Fermi-surface folding expected from the lowered structural symmetry. Optical conductivity $\sigma_1(\omega, T)$ of (e) $\text{Fe}_{1.087}\text{Te}$ and (f) SrFe_2As_2 crossing their magnetostructural phase transitions. Dashed lines indicate expectation from a Dirac cone $G(\omega) = \sigma_1(\omega)d$.

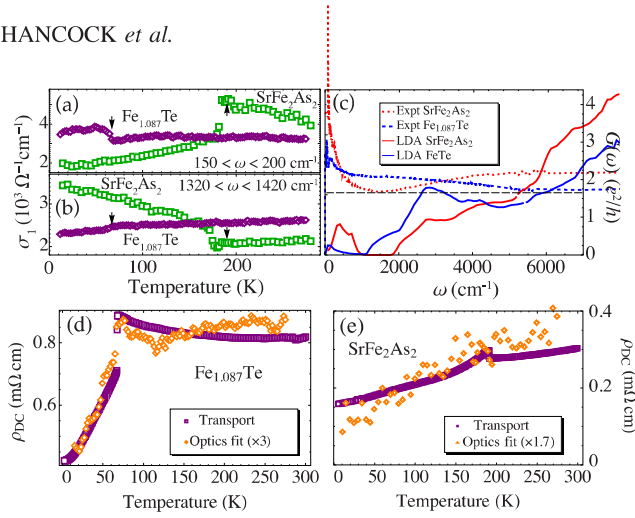


FIG. 2. (Color online) Temperature dependence of σ_1 averaged over a narrow band of (a) far-infrared and (b) midinfrared frequencies. (c) Comparison of the high-temperature conductivity and the interband conductivity calculated from LDA (Ref. 19). Horizontal line marks $G=(\pi/2)e^2/h$. dc resistivity measured by transport (squares) and optically (diamonds) for (d) $\text{Fe}_{1.087}\text{Te}$ and (e) SrFe_2As_2 .

$\sigma(\omega)$ [Fig. 2(c)] than the flat, smooth appearance of the experimental spectra.

Interestingly, the conductance per layer, defined as $G(\omega) = \sigma_1(\omega)d$, where d is the interlayer spacing, is expected to be $(\pi/2)e^2/h$ (Ref. 20) for a Dirac cone spectrum as is observed in carbon.²¹ This type of band structure is predicted^{22,23} and observed^{24,25} for 122 systems in the magnetic phase. Here, we observe a broad, flat conductance of similar magnitude over a wide span of energy and at all temperatures, suggesting that short-range correlations are also present in the paramagnetic phase.

III. DRUDE-LORENTZ MODELING

Figures 2(a) and 2(b) compare the temperature evolution of the conductivity in narrow bands around select frequencies. In each case, a kink at the transition temperature indicates that the optical spectra are influenced by the onset of staggered magnetic order, implying reconstruction of electronic bands in response to the development of the order parameter. While the direction of the effect is opposite for the two systems in both mid-infrared and far-infrared spectral regions, the low-temperature resistivities [Figs. 2(a) and 2(b)] both increase monotonically upon warming to $T \sim T_{ms}$, above which a weaker temperature dependence is observed. Based on dc-transport data alone, it is unclear whether increased scattering or net depletion of carriers is responsible for the resistive changes. We quantify the dynamical extension of the transport behavior to finite frequency by fitting the optical data to a set of Drude-Lorentz oscillators

$$\epsilon(\omega) = \epsilon_\infty + \sum_i \frac{\omega_{p,i}^2}{\omega^2 - \Omega_i^2 - i\gamma_i\omega} = 1 + \frac{4\pi i\sigma(\omega)}{\omega}.$$

This model is appealing because it is Kramers-Kronig consistent and requires only a handful of parameters.

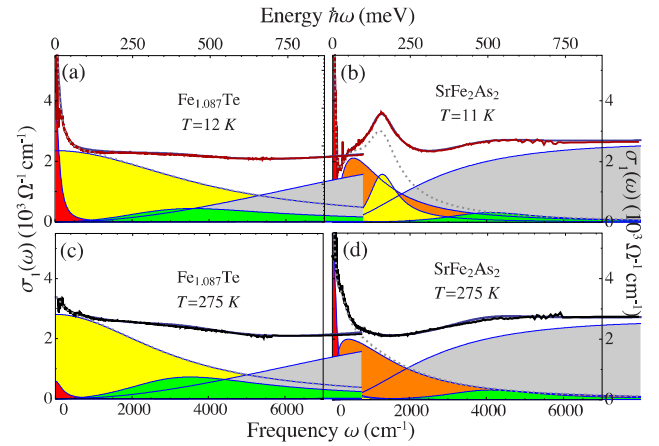


FIG. 3. (Color online) Components of fits to the optical conductivity at high and low temperatures for [(a) and (c)] $\text{Fe}_{1.087}\text{Te}$ and [(b) and (d)] SrFe_2As_2 .

Figure 3 shows results for $\sigma_1(\omega)$ of a fit to a minimalist realization of the model to the reflectivity data at low and high temperatures. In $\text{Fe}_{1.087}\text{Te}$, a minimum of two Drude ($\Omega_i=0$) components were necessary to represent the low-temperature spectra with broad, low-frequency interband contributions at 3500 cm^{-1} and higher. The Drude contributions are clearly separable due to their very different widths γ_i with $i \in \{1, 2\}$. Only quantitative changes distinguish the model in high- and low-temperature phases.

For SrFe_2As_2 , however, with $T < T_{ms}$, two components represent the double-peak structure in addition to a single Drude component. For $T > T_{ms}$, this double-peak structure washes away, a phenomenon discussed in connection to the temperature-induced closing of one^{26,18} or more^{16,17} spin-density wave (SDW) gaps. In an unconstrained fit, the two peaks move to low energy as the temperature is raised and their sum resembles a single wide Drude component and a narrow component (dashed line), like $\text{Fe}_{1.087}\text{Te}$. Thus, at high temperatures, the optical spectra of $\text{Fe}_{1.087}\text{Te}$ and SrFe_2As_2 differ only quantitatively. As the high-temperature phases of these systems are carried into a superconducting state by chemical substitution^{5,6} or application of pressure⁸ or strain,⁷ strong $(\pi, 0)$ spin fluctuations are detected as precursors to superconductivity.^{27,28} In this way, it appears that the low-energy physics of these systems is similar in their paramagnetic states, and the point of strongest departure in their low-energy behavior is along the magnetic phase boundary T_{ms} . One is then confronted with the challenge of understanding the differences in the magnetic ground states and the influences that drive them.

For $\text{Fe}_{1.087}\text{Te}$, Fig. 4(a) shows separately the contributions of the two Drude components to the dc layer conductance $G(0)$. The wide Drude component has a nearly temperature independent value of $2e^2/h$ and is unaffected by the magnetostructural transition. Nearly all of the temperature dependence in transport comes from the parallel conductance channel associated with the narrow Drude component, which grows significantly below T_{ms} . To better understand this behavior, Fig. 4(b) compares the strength $\omega_{p,1}^2$ of the narrow Drude component in each of the two systems. In each case,

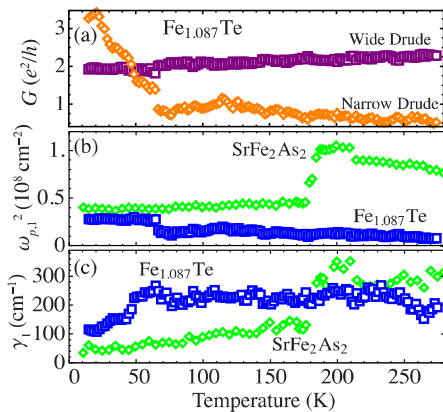


FIG. 4. (Color online) (a) Separate temperature evolution of narrow and wide Drude contributions to the layer conductance of $\text{Fe}_{1.087}\text{Te}$. Comparison of the (b) strengths and (c) widths of the narrow Drude contributions for each of the two systems.

the value of the model $\omega_{p,1}^2$ has a steplike change at the magnetostructural transition and is almost independent of temperature for $T < T_{ms}$. This reflects the fact that the structural transitions are first order,^{1,29} and the formation of electron and hole pockets occurs abruptly at T_{ms} , consistent with ARPES data on BaFe_2As_2 (Ref. 12) and $\text{Fe}_{1.06}\text{Te}$.³⁰ The direction of the step at the transition T_{ms} is the clearest transport-related difference between these two systems: the carrier weight in the 122 system decreases with the onset of magnetic order but the carrier weight of the 11 system increases. This behavioral difference arises from the diverse magnetic-ordering pattern, which has profoundly different effects on zone folding (Fig. 5) and therefore also the topology of the low-temperature Fermi surfaces.

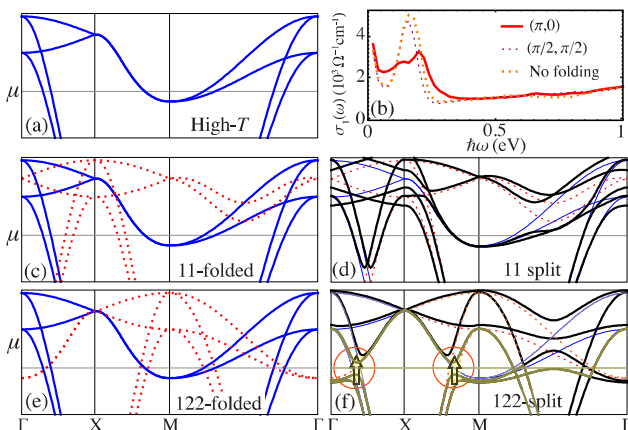


FIG. 5. (Color online) Tight-binding model band structure (Ref. 31) for (a) high-temperature unit cell, (c) folded at $Q_{AF} = (\pi/2, \pi/2)$ and (e) $Q_{AF} = (\pi, 0)$. (d) and (f), respectively, correspond to (c) and (e) with a small mean-field exchange potential included. Allowed optical transitions are indicated by arrows in (f). (b) shows ab -averaged conductivity of a Kubo+five-orbital tight-binding model (Ref. 32) calculation in the high temperature (dashed) and magnetic phases with 200 meV exchange potential with $(\pi, 0)$ (solid) and $(\pi/2, \pi/2)$ (dotted) folding.

IV. DISCUSSION AND CALCULATION

We now relate the qualitative behavior of the higher-frequency optical spectra to these magnetically induced topological changes. Figure 5(a) reproduces a tight-binding model band structure for the high-temperature phase.³¹ Figures 5(c)–5(f) show the effect of translation and mixing of these bands by the antiferromagnetic wave vectors for the 122 [$Q_{SDW} = (\pi, 0)$] and the 11 [$Q_{SDW} = (\pi/2, \pi/2)$] magnetic structures. The 122 folding clearly results in more crossed bands near the Fermi level due to the direct overlap of hole and electron pockets. Near particular degeneracy points along the high-temperature Fermi surface, even small mixing and splitting can open momentum-conserving optical transition pathways, which appear near 550 cm^{-1} in SrFe_2As_2 at low T . If only vertical transitions in the band structure (i.e., those transitions whereby precisely one electron and one hole with overall momentum zero) are considered, the optical spectra should be only weakly influenced by the SDW order, as shown in Fig. 5(b) based on a five-orbital tight-binding model³² simulation with a mean-field exchange potential of 200 meV. Thus, while the different ordering patterns, low-temperature moments, and transition temperatures of these two systems suggest a potentially different strength of the effective exchange potential, the 11 folding has an intrinsically smaller effect on the optical response than the 122 folding, and the salient contrast in optical response can be understood in this way.

We already related the smooth appearance of $\sigma_1(\omega)$ to strong coupling of electron- and hole-excited states to spin fluctuations. Since the spin-fluctuation spectrum of an itinerant (anti)ferromagnet undergoes drastic changes through the magnetic phase transition, this change should then become visible in the optical spectra. Since in the 122 system T_{ms} is high, and the magnetism is typical for a metallic and itinerant material, the largest effect could be expected in this system as compared to $\text{Fe}_{1.087}\text{Te}$, as is indeed the case. The 1300 cm^{-1} feature in the 122 systems has a particularly strong, order-parameter-like temperature dependence below T_{ms} [Fig. 2(b)]. Similar trends have been observed in XFe_2As_2 with $\text{X} = [\text{Ba}, \text{Sr}, \text{Eu}]$ (Refs. 17 and 26). In Ba-122, a low-frequency peak is observed for polarization along and perpendicular to the c axis, but the stronger, high-frequency feature is observed only for polarization perpendicular to c .¹⁸ Furthermore, across systems with different T_{ms} , the low-frequency gap is of appropriate magnitude to consider a mean-field BCS-type SDW gap-crossing (pair-breaking) excitation. As pointed out before,^{16,17,26} the high-energy feature, which appears at 1300 cm^{-1} in SrFe_2As_2 , is highly anomalous.

Based on these considerations, we suggest a magnetic origin for the anomalous feature. Figure 6(a) shows a simplified schematic of the high-temperature band structure. Near the magnetic phase boundary, spin fluctuations provide a dissipation channel which involves an electron traversing a Fermi pocket in a Landau damping process. Below T_{ms} , hybridization and splitting of bands opens an SDW gap excitation pathway, giving rise to the 550 cm^{-1} excitation [Fig. 6(b)]. We assign the second excitation to a process shown schematically in Fig. 6(c). Here, a down-spin electron in an oc-

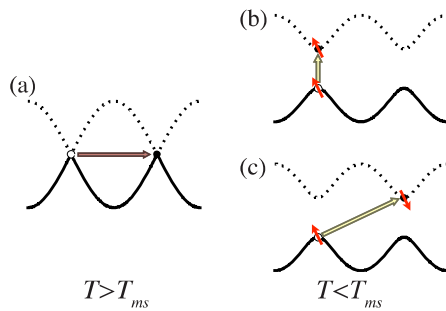


FIG. 6. (Color online) (a) Optical process resulting in a damped fluctuation. (b) Direct and (c) magnon-assisted indirect SDW gap-crossing excitation. Small diagonal arrows indicate spin direction.

cupied state at momentum $-k_F$ undergoes a similar gap-crossing excitation to a state at $+k_F$ while flipping its spin. This is normally disallowed due to the photon momentum and spin-selection rules but can become allowed through the simultaneous emission of a spin-1 magnon of momentum $-2k_F$, so that the overall momentum and spin of the process is conserved. Inelastic neutron scattering³³ has shown that sharp quasi-two-dimensional (2D) spin waves with velocity $v_s \approx 0.28 \text{ eV \AA}$ exist in the low-temperature phase of SrFe_2As_2 . ARPES (Ref. 12) and quantum oscillation¹⁵ experiments detect strong SDW gapping along a hole pocket at Γ and electron pocket at M with gapped sections connected by wave vectors k_c traversing between $0.2\pi/a - 0.5\pi/a$ in the 2D-projected Brillouin zone. Thus, while the average SDW gap excitation appears near 550 cm^{-1} and is roughly consistent with the BCS expectation $2\Delta \sim 3.5k_B T_{ms}$

$\sim 462 \text{ cm}^{-1}$, we expect the magnon-assisted pair-breaking absorption to occur near $k_c v_s \sim 360 - 900 \text{ cm}^{-1}$ higher, which wholly encompasses the observed splitting between high- and low-energy features in SrFe_2As_2 . In this scenario, the low-temperature characteristics of the high-energy peak in SrFe_2As_2 are expected to evolve with temperature as a direct consequence of broadened spin excitations as the temperature is raised, as observed. For $T > T_{ms}$, one expects an overdamped paramagnon response, thus explaining the difficulty in tracking this feature into the high-temperature phase.²⁶ Furthermore, the absence of this feature for c polarization can be a consequence of dimensional considerations through the very different spin wave and band dispersion along the c axis.³³ Future theoretical work is needed to develop this interesting possible mechanism for photon absorption.

In summary, we have observed the influence of spin fluctuations on charge dynamics of two systems closely related to Fe-based superconductors. The spin-charge coupling is most evident at the magnetostructural transitions in these compounds, where transport and charge excitations are sensitive to drastic changes in the spin susceptibility. These observations are robust and likely extend to the superconducting portions of the global phase diagram for Fe-based superconductors.

ACKNOWLEDGMENTS

We acknowledge valuable conversations with A. B. Kuzmenko, I. I. Mazin, and D. Parker. This work was supported by the Swiss National Science Foundation through the NCCR Materials with Novel Electronic Properties (MaNEP).

¹S. Li *et al.*, *Phys. Rev. B* **79**, 054503 (2009).

²W. Bao *et al.*, *Phys. Rev. Lett.* **102**, 247001 (2009).

³G. F. Chen, Z. G. Chen, J. Dong, W. Z. Hu, G. Li, X. D. Zhang, P. Zheng, J. L. Luo, and N. L. Wang, *Phys. Rev. B* **79**, 140509(R) (2009).

⁴Q. Huang, Y. Qiu, W. Bao, M. A. Green, J. W. Lynn, Y. C. Gasparovic, T. Wu, G. Wu, and X. H. Chen, *Phys. Rev. Lett.* **101**, 257003 (2008).

⁵F. C. Hsu *et al.*, *Proc. Natl. Acad. Sci. U.S.A.* **105**, 14262 (2008).

⁶M. Rotter, M. Tegel, and D. Johrendt, *Phys. Rev. Lett.* **101**, 107006 (2008).

⁷Y. Han, W. Y. Li, L. X. Cao, X. Y. Wang, B. Xu, B. R. Zhao, Y. Q. Guo, and J. L. Yang, *Phys. Rev. Lett.* **104**, 017003 (2010).

⁸P. L. Alireza, J. Gillett, Y. T. Chis Ko, C. M. Petrone, J. M. Cole, G. G. Lonzarich, and S. E. Sebastian, *J. Phys.: Condens. Matter* **21**, 012208 (2009).

⁹A. Subedi, L. Zhang, D. J. Singh, and M. H. Du, *Phys. Rev. B* **78**, 134514 (2008).

¹⁰D. J. Singh and M. H. Du, *Phys. Rev. Lett.* **100**, 237003 (2008).

¹¹I. I. Mazin, D. J. Singh, M. D. Johannes, and M. H. Du, *Phys. Rev. Lett.* **101**, 057003 (2008).

¹²M. Yi *et al.*, *Phys. Rev. B* **80**, 024515 (2009).

¹³Y. Xia, D. Qian, L. Wray, D. Hsieh, G. F. Chen, J. L. Luo, N. L.

Wang, and M. Z. Hasan, *Phys. Rev. Lett.* **103**, 037002 (2009).

¹⁴R. Viennois, E. Giannini, D. van der Marel, and R. Černý, *J. Solid State Chem.* **183**, 769 (2010).

¹⁵S. E. Sebastian, J. Gillett, N. Harrison, P. H. C. Lau, D. J. Singh, C. H. Mielke, and G. G. Lonzarich, *J. Phys.: Condens. Matter* **20**, 422203 (2008).

¹⁶W. Z. Hu, J. Dong, G. Li, Z. Li, P. Zheng, G. F. Chen, J. L. Luo, and N. L. Wang, *Phys. Rev. Lett.* **101**, 257005 (2008).

¹⁷D. Wu *et al.*, *Phys. Rev. B* **79**, 155103 (2009).

¹⁸Z. Chen, T. Dong, R. Ruan, B. Hu, B. Cheng, W. Hu, P. Zheng, Z. Fang, X. Dai, and N. Wang, *arXiv:1001.1689* (unpublished).

¹⁹S. Y. Savrasov, *Phys. Rev. B* **54**, 16470 (1996).

²⁰V. P. Gusynin, S. G. Sharapov, and J. P. Carbotte, *Phys. Rev. Lett.* **96**, 256802 (2006).

²¹A. B. Kuzmenko, E. van Heumen, F. Carbone, and D. van der Marel, *Phys. Rev. Lett.* **100**, 117401 (2008).

²²T. Morinari, E. Kaneshita, and T. Tohyama, *arXiv:1003.5469*, *Phys. Rev. Lett.* (to be published).

²³Y. Ran, F. Wang, H. Zhai, A. Vishwanath, and D.-H. Lee, *Phys. Rev. B* **79**, 014505 (2009).

²⁴N. Harrison and S. E. Sebastian, *Phys. Rev. B* **80**, 224512 (2009).

²⁵P. Richard *et al.*, *Phys. Rev. Lett.* **104**, 137001 (2010).

²⁶S. Moon, J. Shin, D. Parker, W. Choi, I. Mazin, Y. Lee, J. Kim,

- N. Sung, B. Cho, S. Khim, J. Kim, K. Kim, and T. Noh, [arXiv:0909.3352](#) (unpublished).
- ²⁷Y. Qiu *et al.*, *Phys. Rev. Lett.* **103**, 067008 (2009).
- ²⁸A. D. Christianson *et al.*, *Nature (London)* **456**, 930 (2008).
- ²⁹A. Jesche *et al.*, *Phys. Rev. B* **78**, 180504 (2008).
- ³⁰Y. Zhang, F. Chen, C. He, L. Yang, B. Xie, Y. Xie, X. Chen, M. Fang, M. Arita, K. Shimada, H. Namatame, M. Taniguchi, J. Hu, and D. Feng, [arXiv:1001.5327](#) (unpublished).
- ³¹S. Raghu, X.-L. Qi, C.-X. Liu, D. J. Scalapino, and S.-C. Zhang, *Phys. Rev. B* **77**, 220503 (2008).
- ³²S. Graser, T. A. Maier, P. J. Hirschfield, and D. J. Scalapino, *New J. Phys.* **11**, 025016 (2009).
- ³³J. Zhao *et al.*, *Phys. Rev. Lett.* **101**, 167203 (2008).